

## Effects of Street-Bottom and Building-Roof Heating on Flow in Three-Dimensional Street Canyons

Jae-Jin KIM<sup>\*1</sup> and Jong-Jin BAIK<sup>2</sup>

<sup>1</sup>*Department of Environmental Atmospheric Sciences, Pukyong National University,  
Busan 608-737, Republic of Korea*

<sup>2</sup>*School of Earth and Environmental Sciences, Seoul National University,  
Seoul 151-742, Republic of Korea*

(Received 30 April 2009; revised 8 September 2009)

### ABSTRACT

Using a computational fluid dynamics (CFD) model, the effects of street-bottom and building-roof heating on flow in three-dimensional street canyons are investigated. The building and street-canyon aspect ratios are one. In the presence of street-bottom heating, as the street-bottom heating intensity increases, the mean kinetic energy increases in the spanwise street canyon formed by the upwind and downwind buildings but decreases in the lower region of the streamwise street canyon. The increase in momentum due to buoyancy force intensifies mechanically induced flow in the spanwise street canyon. The vorticity in the spanwise street canyon strengthens. The temperature increase is not large because relatively cold above-roof-level air comes into the spanwise street canyon. In the presence of both street-bottom and building-roof heating, the mean kinetic energy rather decreases in the spanwise street canyon. This is caused by the decrease in horizontal flow speed at the roof level, which results in the weakening of the mean flow circulation in the spanwise street canyon. It is found that the vorticity in the spanwise street canyon weakens. The temperature increase is relatively large compared with that in the street-bottom heating case, because relatively warm above-roof-level air comes into the spanwise street canyon.

**Key words:** street canyon flow, CFD model, street-bottom heating, building-roof heating, mean kinetic energy, vorticity

**Citation:** Kim, J.-J., and J.-J. Baik, 2010: Effects of street-bottom and building-roof heating on flow in three-dimensional street canyons. *Adv. Atmos. Sci.*, **27**(3), 513–527, doi: 10.1007/s00376-009-9095-2.

### 1. Introduction

One of the atmospheric phenomena attracting attention of urban meteorologists and climatologists is an increase in air temperature over urban areas, so called, the urban heat island. Factors causing urban heat islands are well known, including reduced evaporation, different albedo and heat capacity, and anthropogenic heat production in urban areas (Wallace and Hobbs, 2006). Many previous studies (e.g., Rozoff et al., 2003; Baik et al., 2007b) have contributed to our understanding of the effects of urban heat islands on meteorology and atmospheric environment in and around urban areas in mesoscale perspectives. In addition to these studies, microscale studies of urban heat-

ing effects on flow and pollutant dispersion are needed to better understand urban heating effects and find ways of improving urban atmospheric environment.

In fact, microscale studies of urban flow and pollutant dispersion have been actively performed in the past two decades. Especially, numerical studies using computational fluid dynamics (CFD) models have greatly advanced our understanding of the characteristics of flow and pollutant dispersion in urban street canyons. Main concerns in this research field may be categorized into two. The first is how geometric factors such as building and street aspect ratios influence flow and pollutant dispersion in street canyons (e.g., Hunter et al., 1992). The second is how meteorological conditions such as ambient wind speed and direc-

\*Corresponding author: Jae-Jin KIM, jjkim@pknu.ac.kr

tion, ambient turbulence intensity, and radiative heating/cooling influence flow and pollutant dispersion in street canyons. Radiative heating/cooling effects focus on the effects of street-bottom and building-surface heating by solar radiation on flow and pollutant dispersion in street canyons (e.g., Sini et al., 1996).

Most of structures and ground surfaces in urban areas consist of concrete and asphalt that have low heat capacities, thus causing large daily variations in surface temperature. Therefore, it is important to investigate the effects of variations in thermal environment on flow and pollutant dispersion in street canyons. As for the surface heating, field observations and experimental studies using wind tunnels or water channels have been well undertaken (Uehara et al., 2000; Kovar-Panskus et al., 2002; Kim and Baik, 2005; Richards et al., 2006). On the other hand, numerical studies have been rather limited, with most of them being for two-dimensional street canyons (Sini et al., 1996; Kim and Baik, 1999, 2001; Xie et al., 2006, 2007).

In this study, the effects of street-bottom and building-roof heating on flow in three-dimensional urban street canyons are investigated systematically. For this, a three-dimensional CFD model is employed.

## 2. Numerical model

### 2.1 Model description

The CFD model used in this study is essentially the same as that of Kim (2007). For this study, the thermodynamic energy equation is implemented. The Reynolds-averaged Navier-Stokes equations can be written as

$$\frac{\partial U_i}{\partial t} + U_j \frac{\partial U_i}{\partial x_j} = -\frac{1}{\rho_0} \frac{\partial P^*}{\partial x_i} + \delta_{i3} g \frac{T^*}{T_0} + \nu \frac{\partial^2 U_i}{\partial x_j \partial x_j} - \frac{\partial}{\partial x_j} (\overline{u_i u_j}), \quad (1)$$

$$\frac{\partial U_j}{\partial x_j} = 0, \quad (2)$$

$$\frac{\partial T}{\partial t} + U_j \frac{\partial T}{\partial x_j} = \kappa \frac{\partial^2 T}{\partial x_j \partial x_j} - \frac{\partial}{\partial x_j} (\overline{T' u_j}) + S_h. \quad (3)$$

Here,  $t$ ,  $x_i$ ,  $U_i$ ,  $T$ , and  $P^*$  indicate the time,  $i$ th Cartesian coordinate,  $i$ th mean velocity component, mean temperature, and deviation of pressure from its reference value, respectively.  $u_i$  and  $T'$  are the fluctuations from  $i$ th mean velocity component ( $U_i$ ) and mean temperature ( $T$ ), respectively.  $\rho_0$  is the air density,  $g$  is the acceleration due to gravity,  $\delta_{ij}$  is the Kronecker delta,  $T_0$  is the reference temperature, and  $T^*$  is the deviation of temperature from its reference value.  $\nu$  and  $\kappa$  indicate the kinematic viscosity and thermal diffusivity of air, respectively, and  $S_h$  indicates the source/sink

term of heat.

The Reynolds stress in Eq. (1) and turbulent heat flux in Eq. (3) are parameterized using the eddy diffusivity approach as

$$-\overline{u_i u_j} = \nu_t \left( \frac{\partial U_i}{\partial x_j} + \frac{\partial U_j}{\partial x_i} \right) - \frac{2}{3} \delta_{ij} k, \quad (4)$$

$$-\overline{T' u_j} = \kappa_t \frac{\partial T}{\partial x_j}. \quad (5)$$

Here,  $\nu_t$  and  $\kappa_t$  are the turbulent diffusivities of momentum and heat, respectively, and  $k$  is the turbulent kinetic energy. The turbulent diffusivity of momentum is determined using the turbulent kinetic energy and its dissipation rate ( $\varepsilon$ ).

$$\nu_t = C_\mu \frac{k^2}{\varepsilon}, \quad (6)$$

where  $C_\mu$  is an empirical constant ( $= 0.0845$ ). The turbulent diffusivity of heat is determined using the turbulent diffusivity of momentum and the turbulent Prandtl number ( $Pr_t$ ),  $\kappa_t = \nu_t / Pr_t$ .

The renormalization group (RNG)  $k-\varepsilon$  turbulence closure model used as a turbulence model in this study calculates turbulent kinetic energy and its dissipation rate prognostically.

$$\frac{\partial k}{\partial t} + U_j \frac{\partial k}{\partial x_j} = -\overline{u_i u_j} \frac{\partial U_i}{\partial x_j} + \frac{\delta_{3j} g}{T_0} \overline{T' u_j} + \frac{\partial}{\partial x_j} \left( \frac{\nu_t}{\sigma_k} \frac{\partial k}{\partial x_j} \right) - \varepsilon, \quad (7)$$

$$\frac{\partial \varepsilon}{\partial t} + U_j \frac{\partial \varepsilon}{\partial x_j} = -C_{\varepsilon 1} \frac{\varepsilon}{k} \overline{u_i u_j} \frac{\partial U_i}{\partial x_j} + C_{\varepsilon 1} \frac{\varepsilon}{k} \frac{\delta_{3j} g}{T_0} \overline{T' u_j} + \frac{\partial}{\partial x_j} \left( \frac{\nu_t}{\sigma_\varepsilon} \frac{\partial \varepsilon}{\partial x_j} \right) - C_{\varepsilon 2} \frac{\varepsilon^2}{k} - R, \quad (8)$$

where  $\sigma_k$  ( $= 0.7179$ ),  $\sigma_\varepsilon$  ( $= 0.7179$ ),  $C_{\varepsilon 1}$  ( $= 1.42$ ), and  $C_{\varepsilon 2}$  ( $= 1.68$ ) are empirical constants. The last term on the right hand side in (8) is an extra strain rate term expressed by

$$R = \frac{C_\mu \eta^3 (1 - \eta/\eta_0) \varepsilon^2}{(1 + \beta_0 \eta^3) k}, \quad (9)$$

$$\eta = \frac{k}{\varepsilon} \left[ \left( \frac{\partial U_i}{\partial x_j} + \frac{\partial U_j}{\partial x_i} \right) \frac{\partial U_i}{\partial x_j} \right]^{1/2}. \quad (10)$$

Here, the empirical constants  $\beta_0$  and  $\eta_0$  are 0.012 and 4.377, respectively. The above governing equation set is numerically solved using a finite volume method. To represent the effects of the wall boundaries properly, the wall functions for momentum and heat are implemented, following Versteeg and Malalasekera (1995). The universal distributions for momentum and temperature in this study are further improved compared with those in Kim and Baik (2004) and Baik et al. (2007a) (Table 1).

**Table 1.** The universal distributions of velocity and temperature near wall boundaries.

	universal distribution of near-wall turbulent flows	
	universal velocity ( $u^+$ )	universal temperature ( $T^+$ )
Kim and Baik (2004)	$u^+ = 1/\kappa \ln(y_p/z_0)$	none
Kim (2007)	$u^+ = 1/\kappa \ln(9.8y^+)$	none
Baik et al. (2007a)	$y^+ = y_p c_\mu^{1/4} k^{1/2}/\nu$ $u^+ = 1/\kappa \ln(y_p/z_0)$	$T^+ = Pr_t \{ u^+ + \phi(Pr, Pr_t) \}$ $c_\mu^{1/4} k_P^{1/2} = U_*$
This study	$u^+ = 1/\kappa \ln(9.8y^+)$ $y^+ = y_p c_\mu^{1/4} k^{1/2}/\nu$	$T^+ = Pr_t \{ u^+ + \phi(Pr, Pr_t) \}$

Note: here,  $y_p$  indicates the distance from the near wall node to the solid surface and  $\phi(Pr, Pr_t)$  is the pee-function.

## 2.2 Model validation

The CFD model is validated against the wind tunnel data of Uehara et al. (2000). For this, a numerical simulation is performed in the same building configuration as in Uehara et al. (2000). The ambient air temperature ( $T_a$ ) is 20° and during the model integration the floor-surface temperature ( $T_f$ ) is maintained at 79°. In Fig. 1, simulation results are compared with the results of the wind tunnel experiment of Uehara et al. (2000) and also other numerical simulations (Xie et al., 2006; Baik et al., 2007a). For comparison, the ver-

tical profiles of normalized temperature and horizontal flow speed at the 5th street canyon in the Uehara et al. (2000)'s building configuration are examined. Above  $z/H > 1.2$ , the normalized temperature and horizontal flow speed is slightly overestimated in Xie et al. (2006) but very well reproduced by the present CFD model. Below the roof level, there are relatively large differences among the wind-tunnel and numerical simulation experiments. In Xie et al. (2006), the normalized temperature near the street bottom ( $z/H < 0.05$ ) is underestimated but overestimated in  $z/H > 0.05$  and

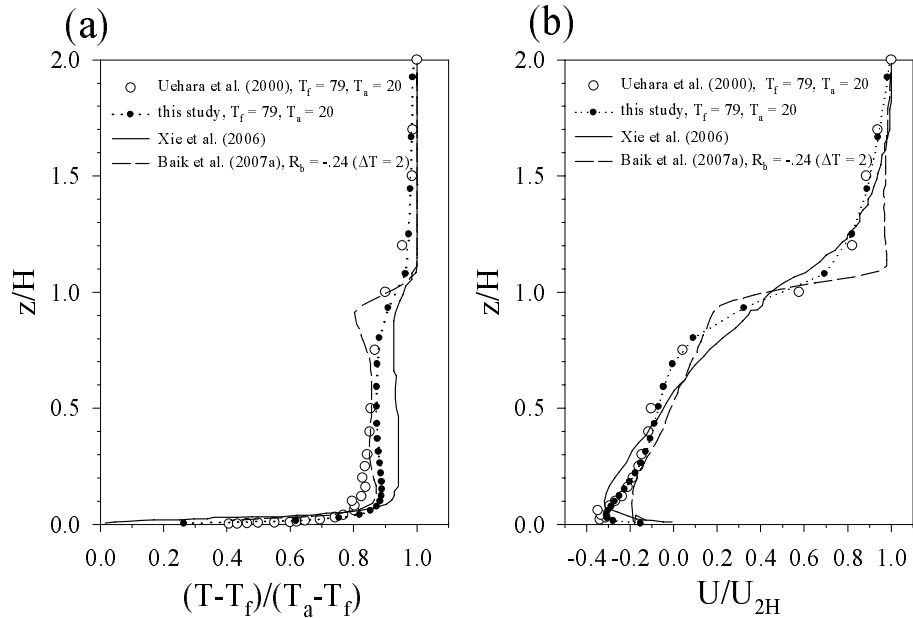


**Fig. 1.** Vertical profiles of measured and simulated (a) temperature and (b) horizontal flow speed. The temperature is normalized by  $(T - T_f)/(T_a - T_f)$  and the horizontal flow speed is normalized by  $U_{2H}$  ( $T_a$ : ambient air temperature at  $z/H = 2$ ,  $T_f$ : floor-surface temperature,  $U_{2H}$ : horizontal flow speed at  $z/H = 2$ , and  $H$ : building height).

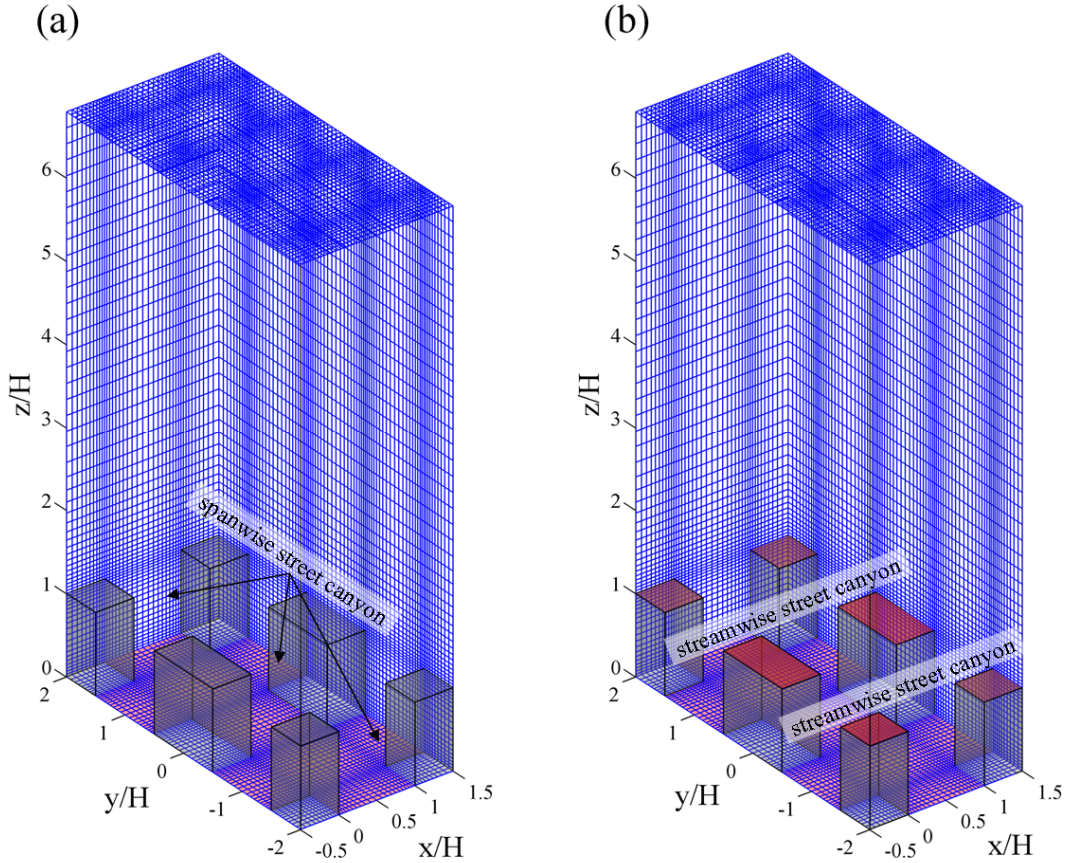


**Fig. 2.** The computational domain and grid system for the (a) street-bottom heating and (b) street-bottom and building-roof heating cases. The surfaces in red color are heated for each case.

the normalized horizontal flow speed is slightly underestimated in  $z/H < 0.08$  but slightly overestimated in  $0.08 < z/H < 0.4$ . Baik et al. (2007a) simulates the normalized temperature profile well but the normalized horizontal flow speed profile poorly. Despite a slight overestimation of the normalized temperature in  $0.08 < z/H < 0.6$ , the present CFD model very closely reproduces the normalized temperature and horizontal flow speed of the wind-tunnel experiment. This suggests that the present CFD model can be reliably used to simulate urban street canyon flow in the presence of heating.

### 2.3 Numerical simulation setup

Figure 2 shows the computational domain and grid system. For this study, a group of buildings with a building height ( $H$ ) of 9.56 m are considered. It is implicitly assumed that this building group is infinitely repeated in the  $x$ - and  $y$ -directions (each building is cubical), so the computational domain is just a basic portion of the domain for repeated building groups. A non-uniform grid system with 40 cells in the  $x$ -direction, 80 cells in the  $y$ -direction, and 60 cells in the  $z$ -direction is employed. The dimension of the

smallest cell is  $0.3 \text{ m} \times 0.3 \text{ m} \times 0.3 \text{ m}$  in the  $x$ -,  $y$ -, and  $z$ -directions, which is situated at each edge of the buildings. The expansion ratio of the grid interval is 1.1. The largest cell dimension is  $0.7 \text{ m} \times 0.7 \text{ m} \times 1.8 \text{ m}$ . The street width is the same as the building height, thus giving building and street-canyon aspect ratios of one.

A main concern in this study is to investigate the effects of street-bottom and building-roof heating on flow in three-dimensional street canyons. For this, three heating configurations are employed: no-heating case, street-bottom heating case (SB), and case with both street-bottom and building-roof heating (BR). In the SB cases, the ground surface is heated (Fig. 2a). In the BR cases, both the ground surface and the building roof are heated (Fig. 2b). The street canyons in the  $x$ - and  $y$ - directions are named the spanwise and streamwise canyons, respectively. The averaged mean kinetic energy, temperature, and vorticity are calculated in the spanwise street canyon in the middle of the domain. An observational study by Niachou et al. (2005) reveals that a maximum difference between the street-bottom temperature and the air temperature can reach  $30^\circ$  in summer days. Keeping this in

mind, six different heating intensities for each of SB and BR cases are considered ( $\Delta T=5^{\circ}\text{C}$ ,  $10^{\circ}\text{C}$ ,  $15^{\circ}\text{C}$ ,  $20^{\circ}\text{C}$ ,  $25^{\circ}\text{C}$ , and  $30^{\circ}\text{C}$ ). Here, the heating intensity ( $\Delta T$ ) is a difference between the street-bottom temperature (building-roof temperature) and the initial air temperature. The initial air temperature is set to  $35^{\circ}$ .

The initial inflow conditions for wind and turbulent kinetic energy and its dissipation rate are specified as

$$U(z) = \frac{U_*}{C_\kappa} \ln \left( \frac{z}{z_0} \right), \quad (11)$$

$$V(z) = 0, \quad (12)$$

$$W(z) = 0, \quad (13)$$

$$k(z) = \frac{1}{C_\mu^{1/2}} U_*^2 \left( 1 - \frac{z}{l} \right)^2, \quad (14)$$

$$\varepsilon(z) = \frac{C_\mu^{3/4} k^{3/2}}{C_\kappa z}. \quad (15)$$

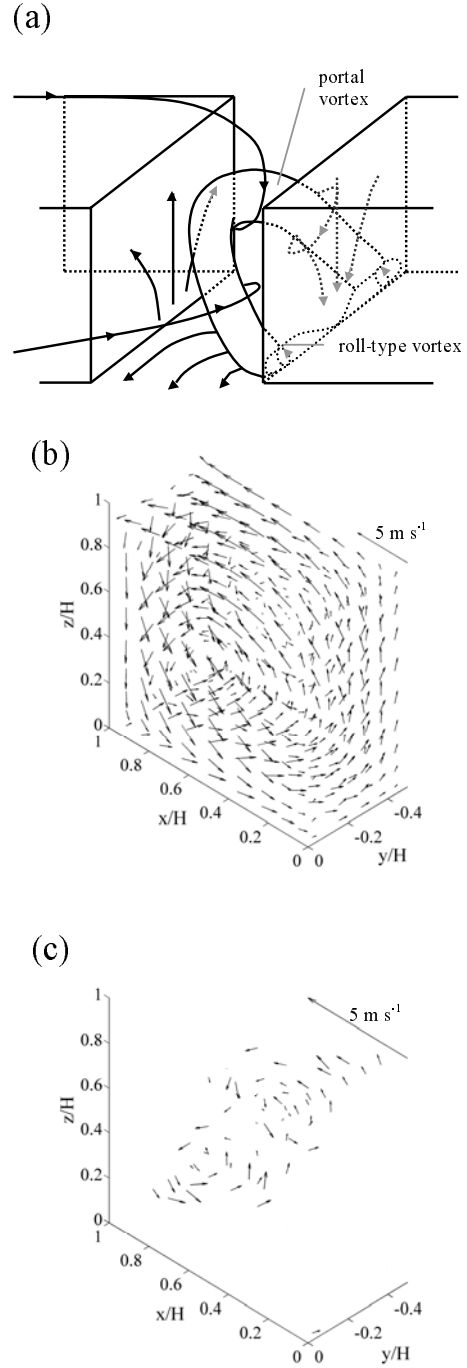
Here,  $U_*$ ,  $z_0$ ,  $l$ , and  $C_\kappa$  are the friction velocity, roughness length ( $=0.05$  m), boundary-layer depth ( $=1000$  m), and von Karman constant ( $=0.4$ ), respectively. The time step used is 0.5 s and the numerical model is integrated up to 1200 s. Simulation results presented below are at  $t=1200$  s. Periodic boundary conditions are applied at lateral boundaries, implying that the building group is repeated in the  $x$ - and  $y$ -directions. A zero-gradient condition is applied at the upper boundary. The wall boundary conditions are applied at the solid surfaces.

### 3. Results and discussion

First, the characteristics of the mean flow in the absence of heating are presented (no-heating case). Then, simulation results of the street-bottom heating case and the case with both street-bottom heating and building-roof heating are analyzed and compared with those of the no-heating case.

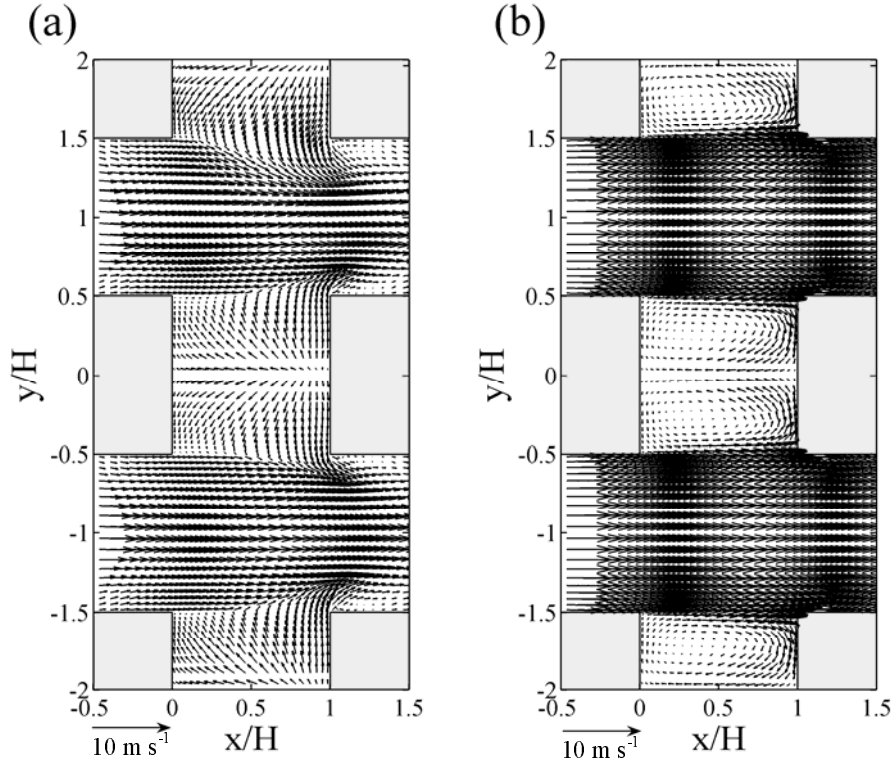
#### 3.1 No-heating case

Figure 3a shows the schematic of the mean flow circulation in a street canyon with street canyon and building aspect ratios of one, which is based on the CFD model simulation (flow regime I in Kim and Baik, 2004). Figure 3b shows the simulated wind vector field in the no-heating case. In Fig. 3c, only a part of the wind vector field in (b) is drawn to clearly represent important mean flow features. The simulated flow field is almost symmetric about  $y/H = 0$  and hence half a



**Fig. 3.** (a) Schematic of the mean flow circulation in a street canyon with street and building aspect ratios of one (from Kim and Baik, 2004) and three-dimensional wind vector fields in the no-heating case [(b) and (c)]. In (c), only a part of the wind vector field in (b) is drawn to clearly represent important mean flow features (portal vortex). The scale bar of wind vector in  $5 \text{ m s}^{-1}$  is indicated in (b) and (c).

region is considered for clarity of the figure. Figure 3a exhibits spiral flows, so called, a portal vortex, appar-



**Fig. 4.** Wind vector fields at  $z/H=(a)$  0.02 and (b) 0.73 in the no-heating case.

ently rounding a tube-shaped core from each side near the lower edges of the downwind building toward the upper central street canyon near the upwind building. The portal vortex is symmetric about the center of the street canyon. An airflow coming into the street canyon curls up, forming the portal vortex in the street canyon (Fig. 3b). Near the upwind building, wind blows upward and outward. Near the downwind building, wind blows downward and inward in the upper layer, but downward and outward in the lower layer. Wind blows outward near the street bottom. These flow features are also ascertained from horizontal wind vector fields at  $z/H=0.02$  and  $0.73$  (Fig. 4). The wind speed decreases in spanwise ( $x$ -directional) street canyons due to the frictional effect of buildings. The decrease in wind speed is large at  $z/H = 0.02$  (near the street bottom). This is because near the street bottom relatively strong outward flow disturbs flow along the streamwise street.

To examine the pattern and intensity of in-canyon vortices, vorticity fields are analyzed. Each vorticity component ( $\omega = \omega_x \mathbf{i} + \omega_y \mathbf{j} + \omega_z \mathbf{k}$ ) is calculated at the center of each grid cell using velocity components. Figure 5 shows the fields of each vorticity component at different cross-sectional planes. In Fig. 5, a positive (negative) vorticity means counter-clockwise (clockwise) rotation in the  $x-y$  and  $y-z$  planes, and

vice versa in the  $x-z$  plane. The magnitude of each vorticity component is large in regions between the above-roof-level and in-canyon flows, where the wind shear is large. The vorticity fields are almost symmetric about  $y/H=0$  (Figs. 5a–c). The magnitude of  $\omega_z$  is large near the mid level of the street canyon and decreases as going downward to the street bottom and going upward to the roof level. Hereafter, a portion of the spanwise street canyon formed by the upwind and downwind buildings, that is, the space of  $0 \leq x/H \leq 1$ ,  $-0.5 \leq y/H \leq 0.5$ , and  $0 \leq z/H \leq 1$  (see Fig. 2), will be called the street canyon just for convenience. The vorticity distributions in the  $x-z$  planes ( $\omega_y$ ) are complicated. At  $y/H = -0.45$ , a region with a large positive vorticity appears in the lower layer near the downwind building due to the existence of a clockwise rotating small vortex and a region with a negative vorticity appears just below the roof level near the downwind building (Fig. 5d). As approaching the center of the street canyon, the area with a negative vorticity migrates downward near the downwind building (Figs. 5e and f). The vorticity fields in the  $y-z$  planes ( $\omega_x$ ) indicate that the extent of two vortices is largest near the upwind building and becomes small as going toward the downwind building (Figs. 5g–i). On the other hand, the magnitude of the vorticity ( $\omega_x$ ) at the vortex cores is small near the upwind building and

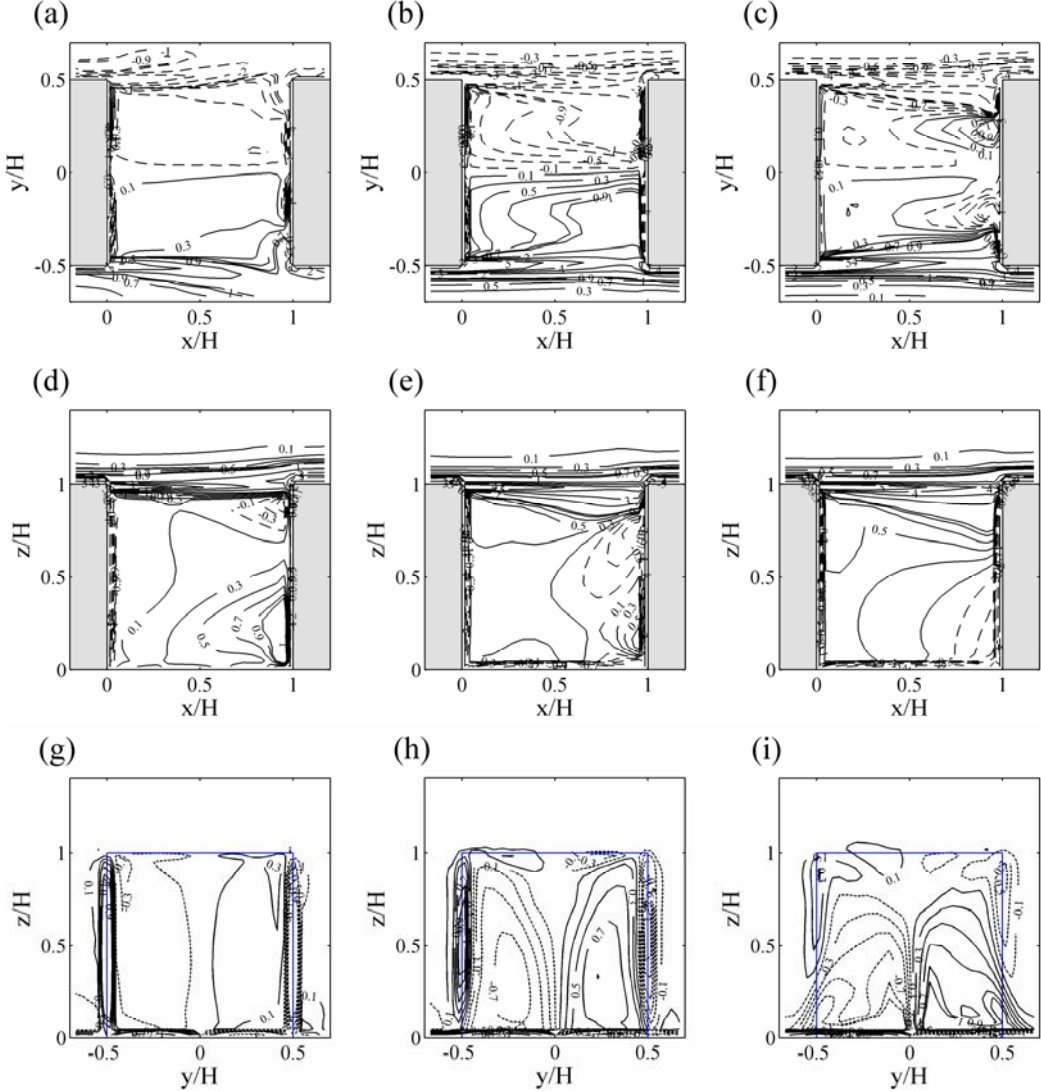


**Fig. 5.** Fields of vorticity components in the  $z$ -direction ( $\omega_z$ ) at  $z/H=(\text{a}) 0.05$ ,  $(\text{b}) 0.46$ , and  $(\text{c}) 0.92$ , in the  $y$ -direction ( $\omega_y$ ) at  $y/H=(\text{d})-0.45$ ,  $(\text{e}) -0.23$ , and  $(\text{f}) -0.04$ , and in the  $x$ -direction ( $\omega_x$ ) at  $x/H=(\text{g}) 0.05$ ,  $(\text{h}) 0.46$ , and  $(\text{i}) 0.92$ . These are for the no-heating case. The contour intervals are  $0.2 \text{ s}^{-1}$  (for  $|\omega| \leqslant 1.1 \text{ s}^{-1}$ ) and  $1 \text{ s}^{-1}$  (for  $|\omega| > 1.1 \text{ s}^{-1}$ ).

large in the lower layer near the downwind building. The results presented above imply that the principal axis of the portal vortex is tilted from each side near the lower edges of the downwind building toward the upper central street canyon near the upwind building.

### 3.2 Street-bottom heating case

There are no significant differences in mean flow pattern between each street-bottom heating case (even the extreme bottom-heating case SB30) and the no-heating case (not shown). Note that SB30 denotes a street-bottom heating case with  $\Delta T=30^\circ$ . Previous studies of two-dimensional street canyon flow (Kim and Baik, 1999, 2005) indicate that the buoyancy force

due to street-bottom heating strengthens vortex by reinforcing mechanically induced upward motion. To investigate the effects of street-bottom heating on flow in three-dimensional street canyons, the mean kinetic energy, temperature, and vorticity fields are analyzed. Here, the mean kinetic energy means the kinetic energy of the mean flow.

Comparisons of vortex intensity at fixed points among the SB cases with different street-bottom heating intensities are not straightforward because the flow structure can be slightly changed due to street-bottom heating. For this reason, the difference in mean kinetic energy between each SB case and the no-heating case is analyzed. Figure 6 shows the fields of difference in

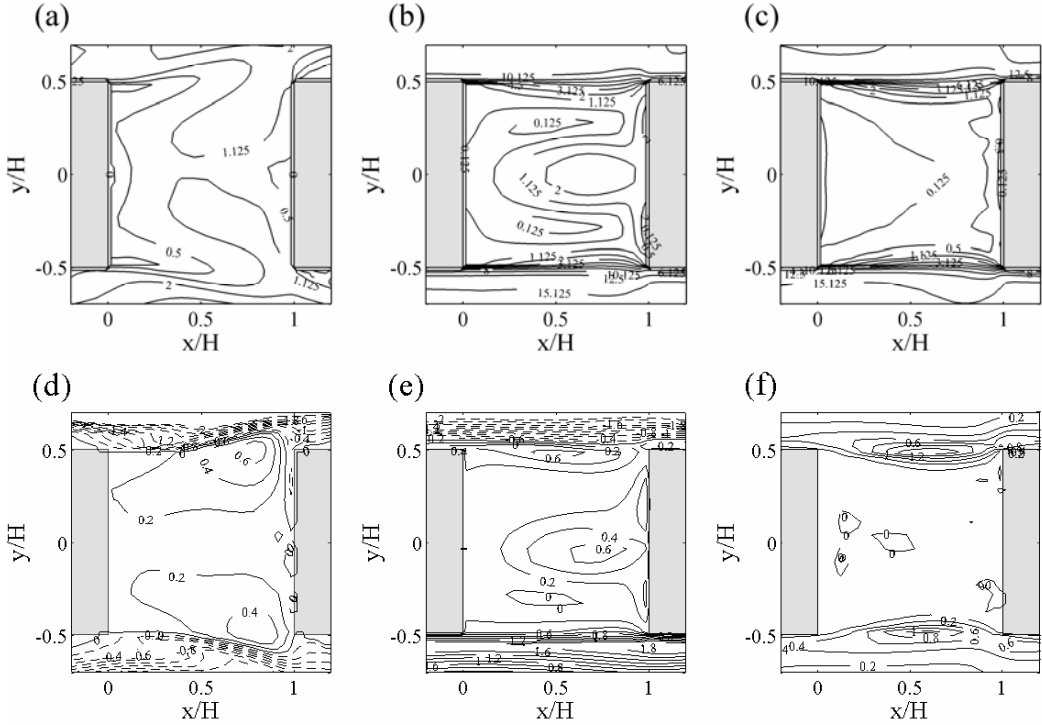


**Fig. 6.** Fields of mean kinetic energy in the SB30 case (upper panels) and difference in mean kinetic energy between the SB30 case and the no-heating case (lower panels) at  $z/H = 0.05$  [(a) and (d)],  $0.46$  [(b) and (e)], and  $0.92$  [(c) and (f)]. The contour interval is  $\alpha^2/2 \text{ m}^2 \text{ s}^{-2}$  ( $\alpha$  varies from 0 to 6 with an interval of 0.5) in (a), (b), and (c) and  $0.2 \text{ m}^2 \text{ s}^{-2}$  in (d), (e), and (f).

mean kinetic energy between the SB30 case and the no-heating case at  $z/H=0.05$ ,  $0.46$ , and  $0.92$ , together with mean kinetic energy fields in the SB30 case. The increase in mean kinetic energy at the street and upper levels is large near  $y/H=0.5$  and  $-0.5$  (Figs. 6d and f). The increase in mean kinetic energy at the mid level is large near  $y/H = 0$  as well as near  $y/H = 0.5$  and  $-0.5$  (Fig. 6e). The difference in mean kinetic energy is found to increase as the street-bottom heating intensity increases. Along the streamwise street canyon, there is relatively little change in mean kinetic energy above the mid level of the street canyon. Also, the decrease in mean kinetic energy appears below the mid level of the streamwise street canyon and it is largest near the street bottom. Note that, at  $y/H < -0.5$  in Fig. 6e, the mean kinetic energy is rather higher than in the no-heating case but it is lower at  $z/H < 0.27$ . This is related to the increase in mean kinetic energy near the bottom of the street canyon. In the no-heating case, the outward flow from the street canyon disturbs flow along the streamwise street canyon (Fig. 4a). The street-bottom heating intensifies vortex circulation in the street canyon. Accordingly, the intensified outward flow near the bottom of the street canyon further disturbs flow along the streamwise street canyon. This results in the weaken-

ing of flow there.

Figure 7 shows normalized temperature fields at  $z/H = 0.05$ ,  $0.46$ , and  $0.92$  in the SB15 and SB30 cases. The temperature is normalized in  $(T - T_a)/\Delta T$ ,  $\Delta T = T_b - T_a$ , where  $T_a$  is the initial air temperature and  $T_b$  is the street-bottom temperature. The normalized temperature patterns in the two different street-bottom heating cases are similar to each other. The normalized temperature at  $z/H = 0.05$  and  $0.46$  is higher in the streamwise street canyon than in the street canyon of  $-0.5 < y/H < 0.5$ . In the street canyon, the normalized temperature at  $z/H=0.92$  does not increase over 10% of  $\Delta T$  (Figs. 7c and f). This is because relatively cold air from the outside comes into the street canyon near the downwind building. Because of the ventilation by the cold above-roof-level air, the normalized temperature is low near the center and downwind region of the street canyon.

An analysis of vorticity fields shows that there are no significant differences in vorticity pattern among the no-heating case and SB cases. The magnitude of each vorticity component increases in the street canyon as the street-bottom heating intensity increases (not shown).

To investigate the variation of the intensity of vorticity in the street canyon with street-bottom heat-

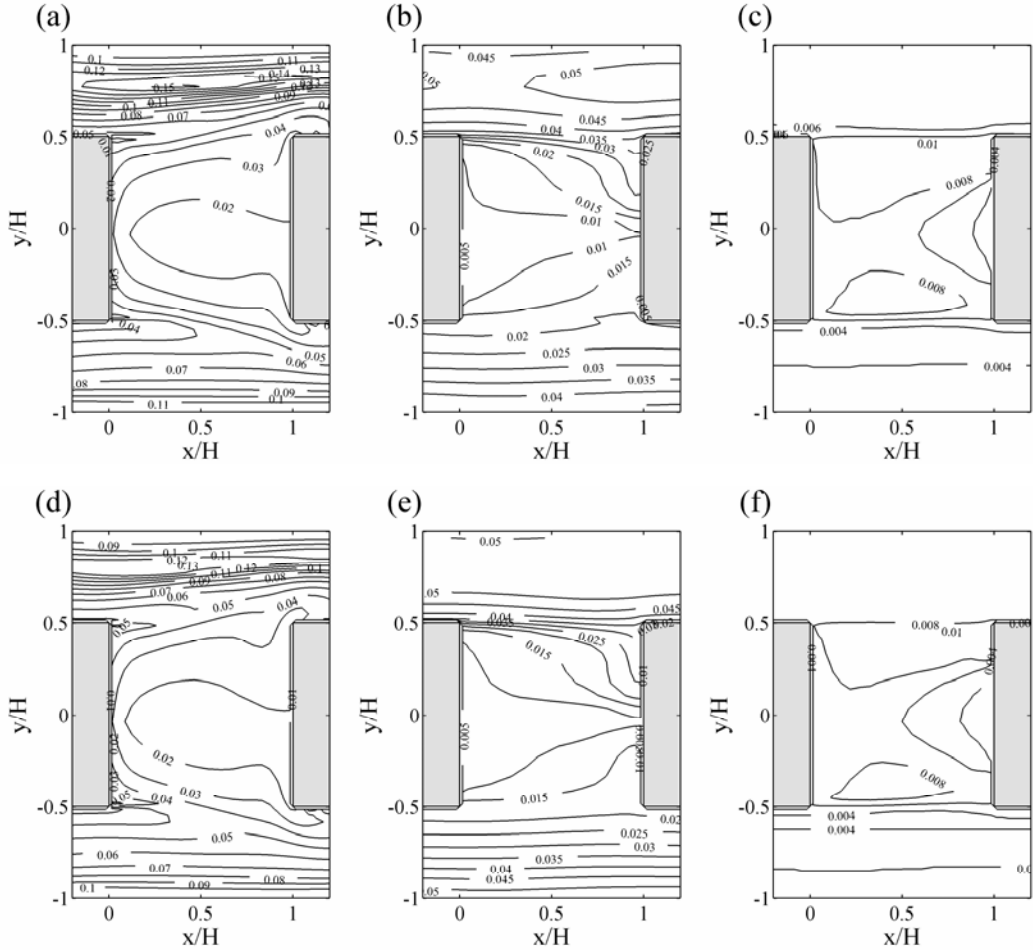


**Fig. 7.** Normalized temperature fields at  $z/H = 0.05$  [(a) and (d)],  $0.46$  [(b) and (e)], and  $0.92$  [(c) and (f)] in the SB15 (upper panels) and SB30 (lower panels) cases. The temperature is normalized by  $(T - T_a)/\Delta T$ ,  $\Delta T = T_b - T_a$  ( $T_a$ : initial air temperature,  $T_b$ : street-bottom temperature). The contour interval is  $0.01$  in (a) and (d),  $0.005$  in (b) and (e), and  $0.002$  in (c) and (f).

ing intensity, the magnitude of the three-dimensional vorticity vector ( $\omega$ ) averaged over the street canyon ( $0 \leq x/H \leq 1$ ,  $-0.5 \leq y/H \leq 0.5$ , and  $0 \leq z/H \leq 1$ ) is analyzed. Table 2 lists the mean kinetic energy, vorticity-vector magnitude, and temperature averaged over the street canyon in the SB cases. Also, listed are percentages of increase/decrease in averaged mean kinetic energy and vorticity-vector magnitude relative to the no-heating case. The averaged vorticity-vector magnitude almost linearly increases with increasing street-bottom heating intensity. The results of the averaged vorticity-vector magnitude in Table 2 indicate that the street-bottom heating strengthens vorticity in the street canyon. In the SB30 case, the increase in averaged vorticity-vector magnitude is largest (7.7% increase relative to the no-heating case). The increase in averaged temperature is very small even in the extreme street-bottom heating case, SB30 ( $0.42^\circ\text{C}$ ). As mentioned above, this is due to the ventilation by rel-

atively cold above-roof-level air. Note that the heating efficiency (defined as the averaged temperature increase divided by  $\Delta T$ ) tends to become small as  $\Delta T$  increases, although the heating efficiency is very small in all the cases. In comparison with the small increase in averaged vorticity-vector magnitude and temperature, the increase in averaged mean kinetic energy is relatively large. The increase is 27.2% in the SB30 case.

### 3.3 Street-bottom and building-roof heating case

The mean flow pattern in each case with both street-bottom and building-roof heating is similar to that in the no-heating case (not shown). Figure 8 shows mean kinetic energy fields in the BR30 case and the fields of difference in mean kinetic energy between the BR30 case and the no-heating case at  $z/H=0.05$ ,  $0.46$ , and  $0.92$ . The pattern of mean kinetic energy

**Table 2.** Mean kinetic energy (MKE), vorticity-vector magnitude (VM), and temperature averaged over the street canyon in the street-bottom heating (SB) cases. Percentages of increase/decrease in averaged MKE and VM relative to the no-heating case are given in parentheses.

Simulations		Averaged MKE ( $\text{m}^2 \text{s}^{-2}$ ) (% increase/decrease)	Averaged VM ( $\text{s}^{-1}$ ) (% increase/decrease)	Averaged temperature (increase, $^{\circ}\text{C}$ )
no heating	$\Delta T=0^{\circ}\text{C}$	0.764	1.55	—
SB05	5 $^{\circ}\text{C}$	0.792 (+3.7)	1.56 (+0.61)	0.08
SB10	10 $^{\circ}\text{C}$	0.822 (+7.6)	1.58 (+1.9)	0.16
SB15	15 $^{\circ}\text{C}$	0.850 (+11.3)	1.60 (+3.2)	0.22
SB20	20 $^{\circ}\text{C}$	0.894 (+17.0)	1.63 (+5.2)	0.29
SB25	25 $^{\circ}\text{C}$	0.932 (+22.0)	1.65 (+6.5)	0.35
SB30	30 $^{\circ}\text{C}$	0.972 (+27.2)	1.67 (+7.7)	0.42

field in the BR30 case is similar to that in the SB30 case, except for  $z/H = 0.05$ , but spatial variations are smaller in the BR30 case than in the SB30 case (Figs. 6 and 8). The fields of difference in mean kinetic energy indicate that additional heating on the building roofs generally decreases mean kinetic energy in the street canyon. Partially, the increase in mean kinetic energy appears near the center of the street canyon ( $0.17 < z/H < 0.88$ ). The increase in mean kinetic energy in the vicinity of the downwind building is mainly caused by increase in  $V^2/2$  ( $V$ : mean velocity component in the streamwise direction). The inward flow from the streamwise street canyon is strengthened at  $z/H > 0.17$ . A further investigation reveals that the decrease in mean kinetic energy near the street bot-

tom ( $z/H < 0.05$ ) is mainly due to decrease in  $V^2/2$  by weakened outward flow and that the decrease in mean kinetic energy near the mid level of the street canyon is caused by the decrease in  $W^2/2$  ( $W$ : mean velocity component in the vertical direction). Additional heating on the building roofs decreases streamwise flow speed and increases vertical flow speed above the roof level (Fig. 9). However, beneath the roof level, the mean kinetic energy increases in the upper region of the street canyon. Despite the partial increase in mean kinetic energy, the decrease in flow speed above the roof level results in the weakening of flow in the street canyon. Consequently, the outward flow near the street bottom of the street canyon becomes weak. Flow near the street bottom along the

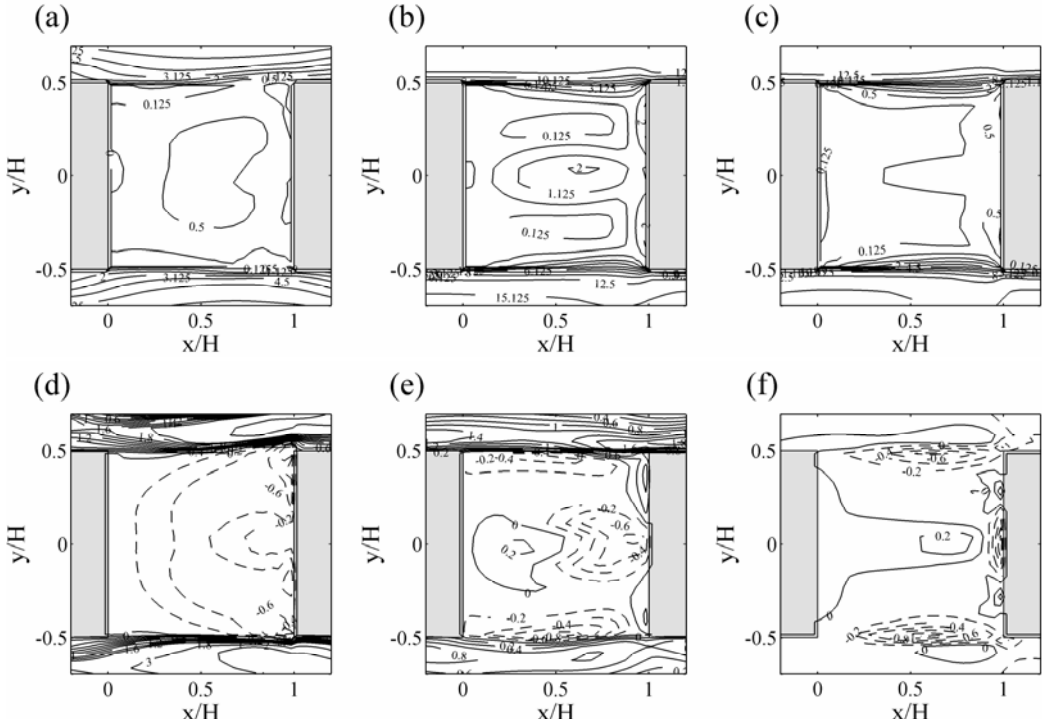
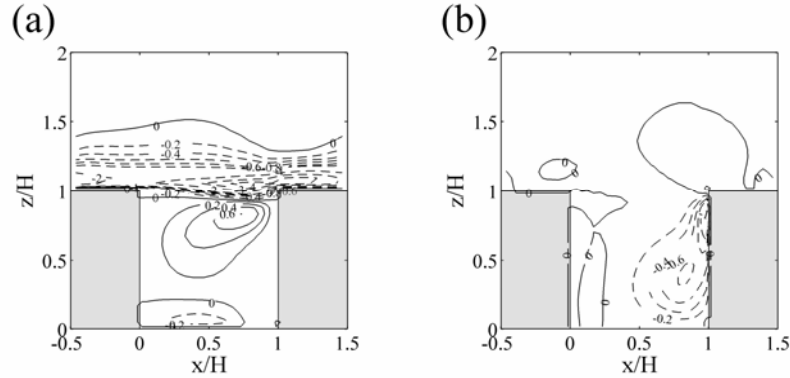
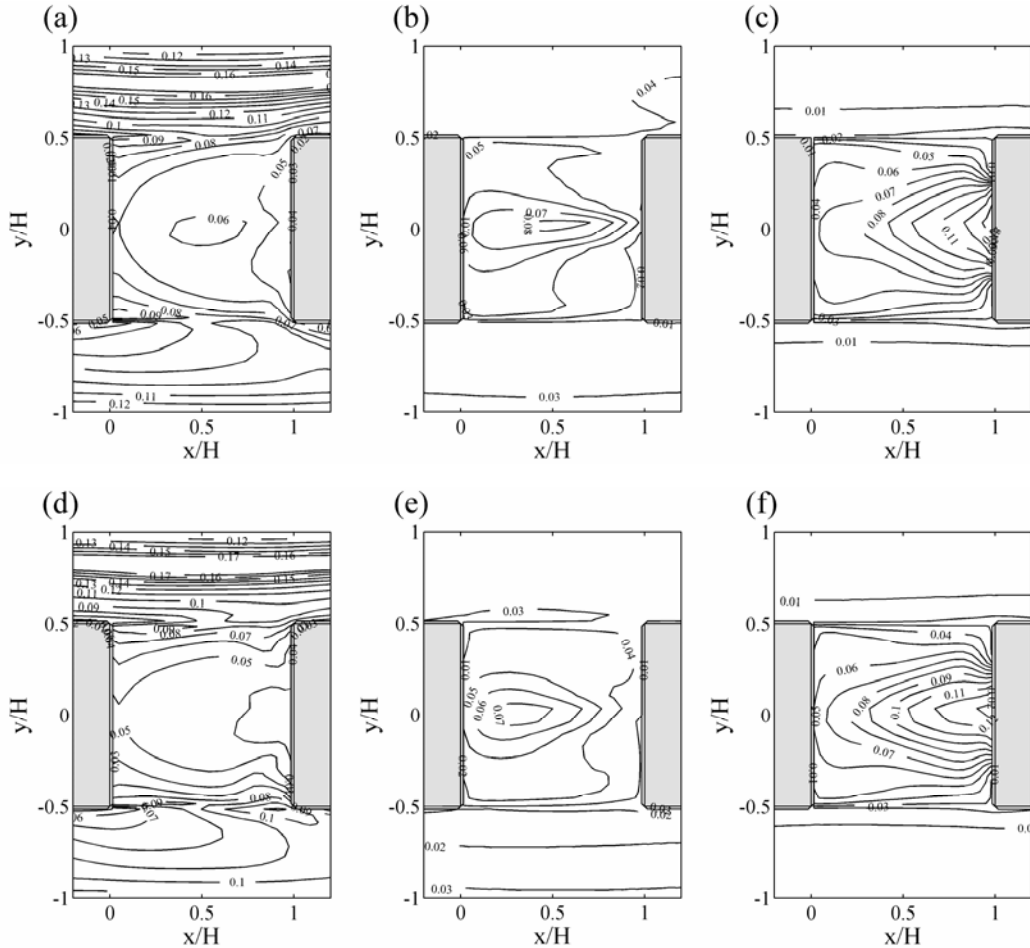


Fig. 8. The same as in Fig. 6 except for the BR30 case.



**Fig. 9.** Fields of differences in (a)  $U^2/2$  and (b)  $W^2/2$  between the BR30 case and the no-heating case. These are at  $y/H = -0.04$ . The contour intervals in (a) and (b) are  $0.2 \text{ m}^2 \text{ s}^{-2}$  (for differences  $\leq 1 \text{ m}^2 \text{ s}^{-2}$ ) and  $1 \text{ m}^2 \text{ s}^{-2}$  (for differences  $> 1 \text{ m}^2 \text{ s}^{-2}$ ).  $U$  is the mean velocity component in the streamwise direction and  $W$  is the mean velocity component in the vertical direction.



**Fig. 10.** The same as in Fig. 7 except for the BR15 (upper panels) and BR30 (lower panels) cases. The contour interval in (a)–(f) is 0.01.

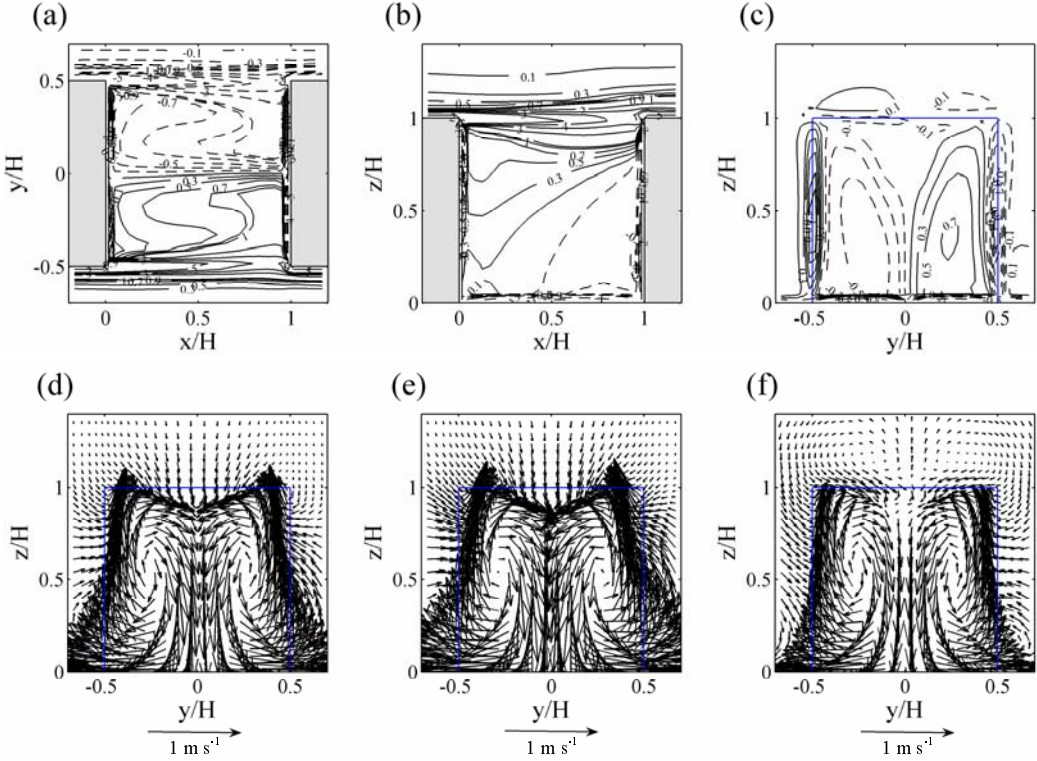


**Fig. 11.** Fields of vorticity components (a) in the  $z$ -direction ( $\omega_z$ ) at  $z/H=0.46$ , (b) in the  $y$ -direction ( $\omega_y$ ) at  $y/H=-0.04$ , and (c) in the  $x$ -direction ( $\omega_x$ ) at  $x/H=0.46$  in the BR30 case and wind vector fields at  $x/H=0.46$  in the (d) no-heating, (e) SB30, and (f) BR30 cases. The contour intervals are  $0.2 s^{-1}$  (for  $|\omega| \leq 1.1 s^{-1}$ ) and  $1 s^{-1}$  (for  $|\omega| > 1.1 s^{-1}$ ).

streamwise street canyon is less disturbed by this outward flow, hence increasing flow speed there.

Figure 10 shows normalized temperature fields at  $z/H = 0.05, 0.46$ , and  $0.92$  in the BR15 and BR30 cases. Near the street bottom, the normalized temperature in the street canyon is lower than that in the streamwise street canyon. Near the roof level, the normalized temperature in the street canyon is higher than that in the streamwise street canyon. The normalized temperature patterns with different  $\Delta T$  are similar to each other. In the street canyon, the normalized temperature is relatively high near the street and roof levels and relatively low near the mid level and its maximum exceeds 13% of  $\Delta T$  near the downwind region where relatively warm above-roof-level air comes into the street canyon. On the other hand, near the mid level, the normalized temperature is low because relatively cold air along the streamwise street canyon comes into the street canyon laterally through both open sides of the street canyon. These results indicate that the temperature distribution is well associated with the mean flow structure.

The vorticity fields show no significant differences in vorticity pattern between each of BR cases and the no-heating case. For example, compare Fig. 5b and

Fig. 11a, Fig. 5f and Fig. 11b, and Fig. 5h and Fig. 11c (Figs. 11a–c is for the BR30 case). Some differences are such that the positive vorticity above the roof level in the  $x$ - $z$  plane ( $\omega_y$ ) migrates upward (Fig. 11b) and positive and negative vorticities additionally appear above the roof level in the  $y$ - $z$  plane ( $\omega_x$ ) (Fig. 11c). The magnitude of each vorticity component in the BR cases is found to decrease as  $\Delta T$  increases (not shown). This is contrary to the result in the SB cases.

In the no-heating and street-bottom heating (SB30) cases, a weak downward motion appears above the roof level (Figs. 11d and e), except for in the vicinity of the downwind building where the upward motion appears due to the flow impingement on the downwind building. In the BR30 case, the building-roof heating induces buoyant upward motion near  $y/H = 0$ , consequently forming two counter-rotating vortices with inward motions to compensate for the buoyant upward motion above the roof level (Fig. 11f). The positive and negative vorticities above the roof level in the BR30 case results from these two counter-rotating vortices. The negative momentum advection by the upward motion above the roof level decreases horizontal flow speed at the roof level.

The mean kinetic energy, vorticity-vector magni-

**Table 3.** The same as in Table 2 except for the cases with both street-bottom and building-roof heating (RB).

Simulations		Averaged MKE ( $\text{m}^2 \text{s}^{-2}$ ) (% increase/decrease)	Averaged VM ( $\text{s}^{-1}$ ) (% increase/decrease)	Averaged temperature (increase, $^{\circ}\text{C}$ )
no heating	$\Delta T=0^{\circ}\text{C}$	0.764	1.55	—
BR05	5 $^{\circ}\text{C}$	0.718 (-6.0)	1.52 (-1.9)	0.32
BR10	10 $^{\circ}\text{C}$	0.688 (-9.9)	1.51 (-2.6)	0.67
BR15	15 $^{\circ}\text{C}$	0.654 (-14.4)	1.49 (-3.9)	0.90
BR20	20 $^{\circ}\text{C}$	0.628 (-17.8)	1.48 (-4.5)	1.17
BR25	25 $^{\circ}\text{C}$	0.608 (-20.4)	1.46 (-5.8)	1.41
BR30	30 $^{\circ}\text{C}$	0.602 (-21.2)	1.47 (-5.2)	1.63

tude, and temperature averaged over the street canyon in the BR cases are listed in Table 3. The averaged vorticity-vector magnitude in the street canyon decreases with increasing  $\Delta T$ . The results of the averaged vorticity-vector magnitude in Table 3 indicate that the street-bottom and building-roof heating weakens vorticity in the street canyon. In the BR25 case, the decrease in averaged vorticity-vector magnitude is largest (5.8% decrease relative to the no-heating case). The increase in averaged temperature is larger in the BR cases than in the SB cases. In the extreme heating case of BR30, the increase in averaged temperature reaches 1.63 $^{\circ}\text{C}$ . The relatively large increase in averaged temperature in the BR cases is due to the incoming of relatively warm above-roof level air into the street canyon. The averaged mean kinetic energy almost linearly decreases with increasing  $\Delta T$ . The decrease in averaged mean kinetic energy is relatively large with a decrease of 21.2% in the BR30 case.

To further identify the characteristics of the street-canyon flows in the presence of heating, two additional numerical simulations are performed for a two-dimensional street-canyon configuration with the street-bottom heating (2D-SB30) and street-bottom and building-roof heating (2D-BR30) cases. The wind-vector fields in the  $xtz$  plane show that the vortex shape in the three-dimensional configuration (Figs. 12a and 12b) is different from that in the two-dimensional configuration (Figs. 12c and 12d). As in previous studies (e.g., Sini et al., 1996; Baik and Kim, 1999), a roll-type vortex is generated and its center is located near the center of the street canyon in the 2D-SB30 and 2D-BR30 cases. Wind in the street canyon is weaker in the 2D-SB30 (2D-BR30) case than in the SB30 (BR30) case. The normalized temperature field in the 2D-SB30 case shows that the temperature is higher near the upwind building due to warm advection by the reverse flow near the street bottom. This feature is similar to that in Kim and Baik (2005)'s watter channel experiment. In the 2D-BR30 case, warm advection from the roof level increases temperature near the downwind building. The temperature in the

spanwise street canyon is overall lower in the three-dimensional configuration due to the incoming of relatively cold air flow outside into the street canyon.

#### 4. Summary and conclusions

In the daytime, street bottom and building surfaces (building walls and building roofs) are heated by solar radiation. Many previous modeling studies have shown that street-bottom and building-surface heating by solar radiation can greatly influence flow and pollutant dispersion in street canyons. However, most previous modeling studies considered two-dimensional street canyons. In this study, we examined the effects of street-bottom and building-roof heating on flow in three-dimensional street canyons using a CFD model. The building and street-canyon aspect ratios were set equal to one. In the presence of street-bottom heating, the mean kinetic energy increases in the spanwise street canyon but decreases in the lower region of the streamwise street canyon as the street-bottom heating intensity increases. In the spanwise street canyon, the thermally induced flow intensifies mechanically induced flow. It was found in the spanwise street canyon that the vorticity strengthens and that the temperature increase is not large because relatively cold above-roof-level air comes into there. In the presence of both street-bottom and building-roof heating, the mean kinetic energy decreases and the mean flow circulation weakens in the spanwise street canyon. The vorticity in the spanwise street canyon was found to weaken. Since relatively warm above-roof-level air comes into the spanwise street canyon, the temperature increase there is relatively large compared with that in the street-bottom heating case.

In this study, we considered simple three-dimensional street canyons with street-canyon and building aspect ratios being one. As an extension of this work, it would be interesting to study the effects of street-bottom and building-surface heating on street canyon flow under configurations with different street-canyon and building aspect ratios and/or uneven

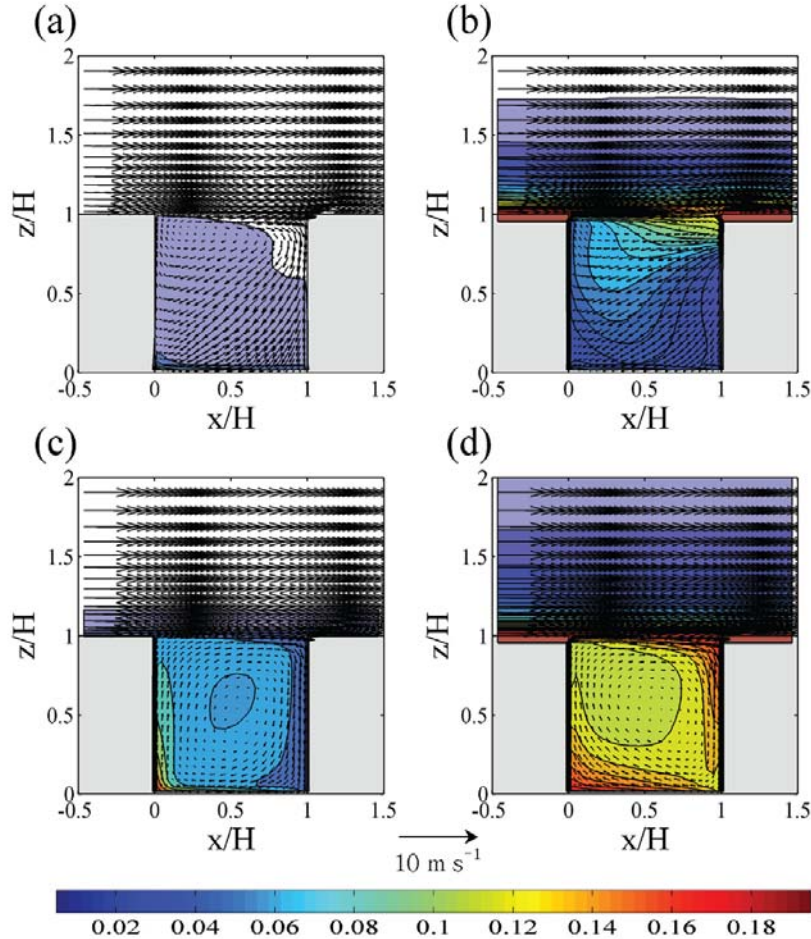


**Fig. 12.** Wind-vector and normalized temperature fields at  $y/H = 0$  in the SB30 [(a) and (c)] and BR30 [(b) and (d)] cases for the three-dimensional (upper panels) and two-dimensional (lower panels) street-canyon configurations. The contour interval is 0.01.

building heights. Also, it would be interesting to study pollutant dispersion in association with flow in three-dimensional street canyons in the presence of street-bottom and building-surface heating.

**Acknowledgements.** The authors are very grateful to two anonymous reviewers for providing valuable comments on this work. This work was funded by the Korea Meteorological Administration Research and Development Program under Grant CATER 2007-3307.

## REFERENCES

- Baik, J.-J., and J.-J. Kim, 1999: A numerical study of flow and pollutant dispersion characteristics in urban street canyons. *J. Appl. Meteor.*, **38**, 1576–1589.  
 Baik, J.-J., Y.-S. Kang, and J.-J. Kim, 2007a: Model-  
 ing reactive pollutant dispersion in an urban street  
 canyon. *Atmos. Environ.*, **41**, 934–949.  
 Baik, J.-J., Y.-H. Kim, J.-J. Kim, and J.-Y. Han, 2007b:  
 Effects of boundary-layer stability on urban heat  
 island-induced circulation. *Theor. Appl. Climatol.*,  
**89**, 73–81.  
 Hunter, L. J., G.T. Johnson, and I.D. Watson, 1992: An  
 investigation of three-dimensional characteristics of  
 flow regimes within the urban canyon. *Atmos. Envi-  
 ron.*, **26B**, 425–432.  
 Kim, J.-J., 2007: The effects of obstacle aspect ratio on  
 surrounding flows. *Atmosphere*, **17**, 381–391. (in Ko-  
 rean with English abstract)  
 Kim, J.-J., and J.-J. Baik, 1999: A numerical study of  
 thermal effects on flow and pollutant dispersion in  
 urban street canyons. *J. Appl. Meteor.*, **38**, 1249–  
 1261.  
 Kim, J.-J., and J.-J. Baik, 2001: Urban street-canyon

- flows with bottom heating. *Atmos. Environ.*, **35**, 3395–3404.
- Kim, J.-J., and J.-J. Baik, 2004: A numerical study of the effects of ambient wind direction on flow and dispersion in urban street canyons using the RNG  $k-\epsilon$  turbulence model. *Atmos. Environ.*, **38**, 3039–3048.
- Kim, J.-J., and J.-J. Baik, 2005: Physical experiments to investigate the effects of street bottom heating and inflow turbulence on urban street-canyon flow. *Adv. Atmos. Sci.*, **22**, 230–237.
- Kovar-Panskus, A., L. Moulinneuf, E. Savory, A. Abdelqari, J.-F. Sini, J.-M. Posant, A. Robins, and N. Toy, 2002: A wind tunnel investigation of the influence of solar-induced wall-heating on the flow regime within a simulated urban street canyon. *Water, Air, and Soil Pollution*, **2**, 555–571.
- Niachou, K., I. Livada, and M. Santamouris, 2005: A study of temperature and wind distribution inside two urban street canyons in Athens. *International Conference on Passive and Low Energy Cooling for the Built Environment*, Santorini, Greece, 125–131.
- Richards, K., M. Schatzmann, and B. Leitl, 2006: Wind tunnel experiments modelling the thermal effects within the vicinity of a single block building with leeward wall heating. *J. Wind Eng. Ind. Aerod.*, **94**, 621–636.
- Rozoff, C. M., W. R. Cotton, and J. O. Adegoke, 2003: Simulation of St. Louis, Missouri, land use impacts on thunderstorms. *J. Appl. Meteor.*, **42**, 716–738.
- Sini, J.-F., S. Anquetin, and P. G. Mestayer, 1996: Pollutant dispersion and thermal effects in urban street canyons. *Atmos. Environ.*, **30**, 2659–2677.
- Uehara, K., S. Murakami, S. Oikawa, and S. Wakamatsu, 2000: Wind tunnel experiments on how thermal stratification affects flow in and above urban street canyons. *Atmos. Environ.*, **34**, 1553–1562.
- Versteeg, H. K., and W. Malalasekera, 1995: *An Introduction to Computational Fluid Dynamics: The Finite Volume Method*. Longman, Malaysia, 198–203.
- Wallace, J. M., and P. V. Hobbs, 2006: *Atmospheric Science: An Introductory Survey*. Academic Press, Oxford, 411pp.
- Xie, X., C.-H. Liu, D. Y. C. Leung, and M. K. H. Leung, 2006: Characteristics of air exchange in a street canyon with ground heating. *Atmos. Environ.*, **40**, 6396–6409.
- Xie, X., C.-H. Liu, and D. Y. C. Leung, 2007: Impact of building facades and ground heating on wind flow and pollutant transport in street canyons. *Atmos. Environ.*, **41**, 9030–9049.